



A Barotropic Model of Eddy Saturation

NAVID C. CONSTANTINO

Scripps Institution of Oceanography, University of California, San Diego, La Jolla, California

(Manuscript received 13 September 2017, in final form 23 December 2017)

ABSTRACT

Eddy saturation refers to a regime in which the total volume transport of an oceanic current is insensitive to the wind stress strength. Baroclinicity is currently believed to be the key to the development of an eddy-saturated state. In this paper, it is shown that eddy saturation can also occur in a purely barotropic flow over topography, without baroclinicity. Thus, eddy saturation is a fundamental property of barotropic dynamics above topography. It is demonstrated that the main factor controlling the appearance or not of eddy-saturated states in the barotropic setting is the structure of geostrophic contours, that is, the contours of f/H (the ratio of the Coriolis parameter to the ocean's depth). Eddy-saturated states occur when the geostrophic contours are open, that is, when the geostrophic contours span the whole zonal extent of the domain. This minimal requirement for eddy-saturated states is demonstrated using numerical integrations of a single-layer quasi-geostrophic flow over two different topographies characterized by either open or closed geostrophic contours with parameter values loosely inspired by the Southern Ocean. In this setting, transient eddies are produced through a barotropic–topographic instability that occurs because of the interaction of the large-scale zonal flow with the topography. By studying this barotropic–topographic instability insight is gained on how eddy-saturated states are established.

1. Introduction

The Southern Ocean, and in particular the Antarctic Circumpolar Current (ACC), are key elements of the climate system. The ACC is driven by a combination of strong westerly winds and buoyancy forcing. [Straub \(1993\)](#) advanced the remarkable hypothesis that the equilibrated ACC zonal transport should be insensitive to the strength of the wind stress forcing. This insensitivity was later verified in eddy-resolving ocean models of the Southern Ocean and is now referred to as eddy saturation (e.g., [Hallberg and Gnanadesikan 2001](#); [Tansley and Marshall 2001](#); [Hallberg and Gnanadesikan 2006](#); [Hogg et al. 2008](#); [Farneti et al. 2010](#); [Meredith et al. 2012](#); [Morrison and Hogg 2013](#); [Munday et al. 2013](#); [Abernathey and Cessi 2014](#); [Farneti et al. 2015](#); [Marshall et al. 2017](#)). Some indications of eddy saturation are seen in observations ([Böning et al. 2008](#); [Firing et al. 2011](#)).

There is evidence that the strength of the westerly winds over the Southern Ocean, which force the ACC, is increasing ([Thompson and Solomon 2002](#); [Marshall 2003](#);

[Yang et al. 2007](#); [Swart and Fyfe 2012](#)). Recently, [Hogg et al. \(2015\)](#) using satellite altimetry data identified that along with the strengthening of the westerlies comes also a linear trend of the Southern Ocean surface eddy kinetic energy (EKE), while the ACC zonal transport remains insensitive or even has decreased. This way, [Hogg et al. \(2015\)](#) concluded that the ACC is in an eddy-saturated state. Given the strengthening of the Southern Ocean westerly winds over the last decades, and the potential enhanced strengthening under global warming forcing ([Bracegirdle et al. 2013](#)), the question that naturally arises is how will the ACC transport respond? Thus, understanding the mechanisms behind eddy saturation is particularly relevant. This paper attempts to shed some more insight in the mechanism underlying eddy saturation.

Initially the explanation for eddy saturation given by [Straub \(1993\)](#) relied on baroclinic processes and on the existence channel walls. In the following detailed models of [Nadeau and Straub \(2009, 2012\)](#), [Nadeau et al. \(2013\)](#), and [Nadeau and Ferrari \(2015\)](#), the arguments for explaining eddy saturation were barotropic in heart. Specifically, [Nadeau and Ferrari \(2015\)](#) argued that the circulation can be decomposed to a circumpolar mode

Corresponding author: Navid Constantinou, navid@ucsd.edu

DOI: 10.1175/JPO-D-17-0182.1

© 2018 American Meteorological Society. For information regarding reuse of this content and general copyright information, consult the [AMS Copyright Policy](#) (www.ametsoc.org/PUBSReuseLicenses).

and a gyre mode (with the latter not contributing to the total transport). [Nadeau and Ferrari \(2015\)](#) showed that the wind stress curl spins barotropic gyres and, furthermore, that an increase of wind stress strength spins up the gyres while leaving the circumpolar mode intact; thus, the transport remains insensitive. Still, though, all those explanations relied in baroclinic instability for producing transient eddies to transfer the momentum from the surface of the ocean down to the bottom. On the other hand, [Marshall et al. \(2017\)](#) and [Mak et al. \(2017\)](#) recently showed that eddy saturation can emerge as a result of an eddy flux parameterization that was introduced by [Marshall et al. \(2012\)](#). In agreement with [Straub \(1993\)](#), [Marshall et al. \(2017\)](#) also relate the production of EKE to the vertical shear of the zonal mean flow. Again, baroclinic instability is identified as the main source of EKE. In this paper, we show that eddy saturation can be observed without baroclinic eddies, without channel walls, and without any wind stress curl, that is, without any gyres.

According to [Johnson and Bryden \(1989\)](#), different density layers are coupled via interfacial form stress that transfers momentum downward from the sea surface to the bottom. At the bottom it is topographic form stress that transfers momentum from the ocean to the solid earth ([Munk and Palmén 1951](#)). Note that only the standing eddies result in time-mean topographic form stress. Thus, it seems reasonable that topography should play a dominant role in understanding what sets up the total vertically integrated transport. There is a consensus that topography acts as the main sink in the zonal momentum balance [in agreement with [Munk and Palmén \(1951\)](#)]. But can the topography also have an active role in setting up the momentum balance, for example, by shaping the standing eddy field and its associated form stress? [Abernathey and Cessi \(2014\)](#) argued in favor of the active role the topography can have in setting up the momentum balance. They showed that isolated topographic features result in localized absolute baroclinic instability (i.e., baroclinic eddy growth in situ above the topographic features) and an associated almost-barotropic standing eddy field pattern. Transient eddies are suppressed away from the topographic features. Furthermore, [Abernathey and Cessi \(2014\)](#) demonstrated that the topographic feature results in the thermocline being shallower and the isopycnal slope being smaller compared to the flat-bottom case. Thus, the usual arguments assuming that the isopycnal slopes are so steep as to be marginal with respect to the flat-bottomed baroclinic instability cannot be invoked to explain the ACC equilibration (and thus neither eddy saturation) in a model configuration with localized topography. In addition, [Thompson and Naveira Garabato \(2014\)](#), and more recently [Youngs et al. \(2017\)](#), further emphasized the role

of the standing eddies (or standing meanders) in setting up the momentum balance and the ACC transport. In this paper, we emphasize the role of the standing eddies and their form stress in determining transport in an eddy-saturated regime within a barotropic setting.

Lately, there has been increasing evidence arguing for the importance of the barotropic processes in determining the ACC transport. [Ward and Hogg \(2011\)](#) studied the ACC equilibration using a multilayer primitive equation wind-driven model with an ACC-type configuration starting from rest. Following turn-on of the wind a strong barotropic current forms within several days that is able to transfer most of the imparted momentum to the bottom; only after several years does the momentum start being transferred vertically via interfacial form stress. The fast response is that a bottom pressure signal arises a few days after turn-on, and the associated topographic form stress couples the ocean to the solid earth. Subsequently, for about 10 years, and contrary to the statistical equilibrium scenario described by [Johnson and Bryden \(1989\)](#), interfacial form stress transfers momentum vertically from the bottom upward. At equilibrium both eastward momentum is transferred from the surface downward and also westward momentum from the bottom upward. On the other hand, studies using in situ velocity measurements, satellite altimetry, and output from the Southern Ocean State Estimate (SOSE) also argue in favor of the importance of the bottom velocity component of the ACC transport, which comes about from the barotropic component of the flow¹ ([Rintoul et al. 2014](#); [Peña Molino et al. 2014](#); [Masich et al. 2015](#); [Donohue et al. 2016](#)). For example, using measurement from the cDrake experiment, [Donohue et al. \(2016\)](#) estimated that the bottom velocity component of the ACC transport accounts for about 25% of the total transport.

[Constantinou and Young \(2017\)](#) discussed the role of standing eddies using a simple barotropic model forced by an imposed steady wind stress and retarded by a combination of bottom drag and topographic form stress ([Hart 1979](#); [Davey 1980](#); [Holloway 1987](#); [Carnevale and Frederiksen 1987](#)). [Constantinou and Young \(2017\)](#) used a random, monoscale topography and argued that a critical requirement for eddy saturation is that the ratio of planetary potential vorticity (PV) gradient to topographic PV gradient is large enough so that the geostrophic contours (i.e., the contours of the planetary PV

¹ Traditionally, the baroclinic component of the flow is obtained through the thermal–wind relationship after assuming zero flow at the bottom. Thus, any transport caused by the bottom flow is not thought as part of the baroclinic component of the ACC transport.

plus the topographic contribution to PV) are open in the zonal direction. Here, we demonstrate that what matters for eddy saturation is not the actual value of the ratio of planetary PV over topographic PV but rather the structure of the geostrophic contours themselves.

The main goal of the present paper is to provide insight on how eddy saturation is established in this barotropic setting. We do that by comparing numerical results using two simple sinusoidal topographies. We show that this barotropic model without baroclinic instability can exhibit impressive eddy saturation, provided that the geostrophic contours are open (see section 3). We do not claim here that baroclinic processes are not important for setting up the momentum balance in the Southern Ocean. Instead, we emphasize the role of barotropic dynamics and the fact that we can still observe eddy saturation without baroclinicity. In this barotropic model, transient eddies arise as an instability caused by the interaction of the large-scale zonal flow with the topography. The simple topography used here allows us to study in detail this barotropic–topographic instability that gives rise to transient eddies and thus provide insight on how eddy-saturated states appear (see section 5). We show, in this way, that topography does not only have a passive role in setting the zonal momentum balance by acting as the main sink of zonal momentum, but it can also have an active role by producing transient eddies that shape the standing eddy field and its associated form stress.

2. Setup

Consider the quasigeostrophic dynamics of a barotropic fluid of depth $H - h(x, y)$ on a beta plane. The fluid velocity consists of a large-scale, domain-averaged zonal flow $U(t)$ along the zonal x direction plus smaller-scale eddies with velocity (u, v) . The eddy component of the flow is derived via an eddy streamfunction $\psi(x, y, t)$ through $(u, v) = (-\partial_y\psi, \partial_x\psi)$; the streamfunction of the total flow is $-U(t)y + \psi(x, y, t)$. The relative vorticity of the flow is $\nabla^2\psi$, where $\nabla^2 \stackrel{\text{def}}{=} \partial_x^2 + \partial_y^2$, and the quasigeostrophic potential vorticity (QGPV) of the flow is

$$f_0 + \beta y + \eta + \nabla^2\psi. \tag{1}$$

In (1), f_0 is the Coriolis parameter at the center of the domain, β is the planetary PV gradient, and $\eta(x, y) \stackrel{\text{def}}{=} f_0 h(x, y)/H$ is the topographic contribution to QGPV or simply the topographic PV. The QGPV and the large-scale flow evolve through

$$\partial_t \nabla^2\psi + J(\psi - Uy, \nabla^2\psi + \eta + \beta y) = -D\nabla^2\psi, \quad \text{and} \tag{2a}$$

$$\partial_t U = F - \mu U - \langle \psi \partial_x \eta \rangle, \tag{2b}$$

(Hart 1979; Davey 1980; Holloway 1987; Carnevale and Frederiksen 1987). In (2a), J is the Jacobian, $J(a, b) \stackrel{\text{def}}{=} (\partial_x a)(\partial_y b) - (\partial_y a)(\partial_x b)$, and $D \stackrel{\text{def}}{=} \mu + \nu_4 \nabla^4$ is the dissipation operator, which includes linear Ekman drag μ and hyperviscosity ν_4 used for numerical stability. On the right of (2b), $\langle \psi \partial_x \eta \rangle$ is the topographic form stress, with angle brackets denoting an average over the domain. The large-scale flow $U(t)$ in (2b) is forced by the constant $F = \tau/(\rho_0 H)$, where τ is the uniform surface zonal wind stress, and ρ_0 is the reference density of the fluid, while is being retarded by a combination of bottom drag and topographic form stress. Being constant over the whole domain, the wind stress has no curl. The domain is periodic in both the zonal and the meridional directions, with size $2\pi L \times 2\pi L$. Following Bretherton and Karweit (1975), we have in mind a midocean region that is smaller than ocean basins but much larger than the length scale of ocean macroturbulence. The role of hyperviscosity is limited only to the removal of small-scale enstrophy. Thus, the hyperviscosity has a very small effect on larger scales, and energy dissipation is mainly due to drag μ .

The model formulated in (2) is the simplest model that can be used to investigate beta-plane turbulence above topography driven by a large-scale zonal wind stress applied at the surface of the fluid. It has been used in the past for studying the interaction of zonal flows with topography (Hart 1979; Davey 1980; Holloway 1987; Carnevale and Frederiksen 1987) and recently by Constantinou and Young (2017) for studying the geostrophic flow regimes above random monoscale topography.

Inspired by the Southern Ocean, we take $L = 775$ km, $H = 4$ km, $\rho_0 = 1035$ kg m⁻³, $f_0 = -1.26 \times 10^{-4}$ s⁻¹, and $\beta = 1.14 \times 10^{-11}$ m⁻¹ s⁻¹. Also, we take $h_{\text{rms}} \stackrel{\text{def}}{=} \sqrt{\langle h^2 \rangle} = 200$ m, which implies that $\eta_{\text{rms}} = 6.3 \times 10^{-6}$ s⁻¹. For Ekman drag we use $\mu = 6.3 \times 10^{-8}$ s⁻¹ $\approx (180 \text{ day})^{-1}$ (Arbic and Flierl 2004).

Results are reported using two sinusoidal topographies:

$$\eta^{\parallel} = \sqrt{2}\eta_{\text{rms}} \cos(14x/L) \quad \text{and} \tag{3a}$$

$$\eta^{\times} = 2\eta_{\text{rms}} \cos(10x/L) \cos(10y/L). \tag{3b}$$

Both topographies in (3) are monoscale, that is, they are characterized by a single length scale $\ell_{\eta} = \eta_{\text{rms}}/|\nabla\eta|_{\text{rms}}$, which is

$$\ell_{\eta}^{\parallel} \approx \ell_{\eta}^{\times} = 0.071L = 55.03 \text{ km}.$$

Thus, for both topographies the ratio of planetary PV gradient to topographic PV gradient is $\beta/|\nabla\eta|_{\text{rms}} = 0.1$.

An important factor controlling the behavior of the flow is the structure of the geostrophic contours, that is, the

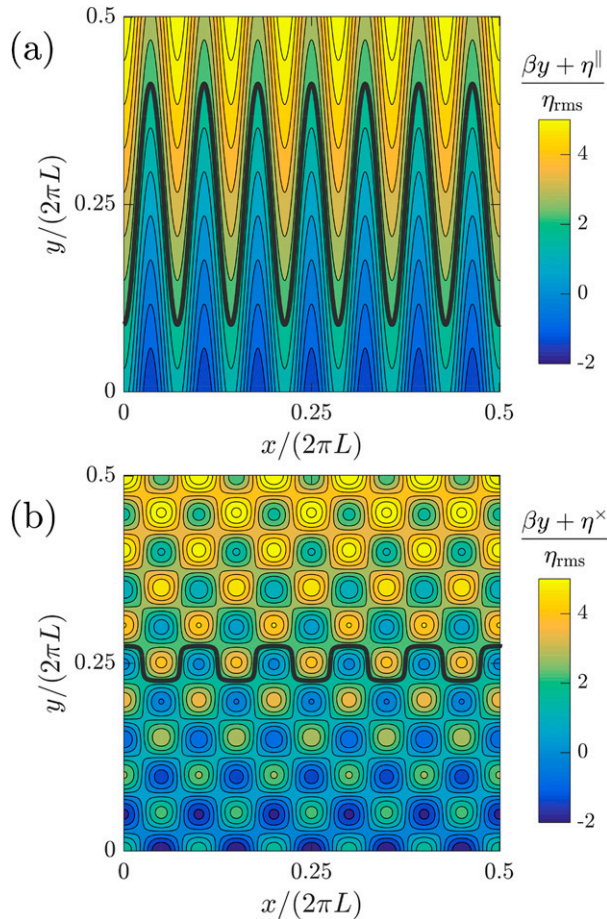


FIG. 1. The structure of the geostrophic contours $\beta y + \eta$ for the two types of topographies used in this paper: (a) η^{\parallel} and (b) η^{\times} . For both cases $\beta \ell_{\eta} / \eta_{\text{rms}} = 0.1$. An open geostrophic contour for each case is marked with a thick curve. The case $\beta y + \eta^{\parallel}$ consists of only open geostrophic contours, while $\beta y + \eta^{\times}$ consists of mostly closed ones. (Only a quarter of the flow domain is shown.)

level sets of $\beta y + \eta(x, y)$. Figure 1 shows the structure of geostrophic contours for the two topographies η^{\parallel} and η^{\times} using the parameters given above. Here, we distinguish between open and closed geostrophic contours. Open geostrophic contours span the full zonal extent of the domain; see, for example, the two contours marked with thick black curves in each panel of Fig. 1. For any nonzero β , all geostrophic contours for topography η^{\parallel} are open, while for topography η^{\times} there exist both closed as well as open geostrophic contours. However, for topography η^{\times} open geostrophic contours, such as the one shown in Fig. 1b, are only found in the vicinity of narrow channels that span the horizontal extent of the domain snaking around local maxima and minima of $\beta y + \eta^{\times}$. We say, therefore, that η^{\times} is characterized by closed geostrophic contours.

It is useful to decompose the eddy streamfunction ψ into time-mean standing eddies with streamfunction $\bar{\psi}$ and residual transient eddies ψ' so that

$$\psi(x, y, t) = \bar{\psi}(x, y) + \psi'(x, y, t),$$

where the time mean is $\bar{\psi} \stackrel{\text{def}}{=} \lim_{T \rightarrow \infty} (1/T) \int_{t_0}^{t_0+T} \psi(x, y, t') dt'$, with t_0 , the time the flow needs to reach a statistically steady state. Similarly, all fields can be decomposed into time-mean and transient components, for example, $U(t) = \bar{U} + U'(t)$. We are interested in how the time-mean, large-scale flow \bar{U} , which is directly related to the time-mean total zonal transport, depends on wind stress forcing F .

All solutions presented in this paper employ 512^2 grid points; this resolution allows about six grid points within ℓ_{η} . We have verified that results remain unchanged with double the resolution. The hyperviscosity coefficient is set to $\nu_4 = 2.27 \times 10^9 \text{ m}^4 \text{ s}^{-1}$. Model (2) is evolved using the exponential, time-differencing, fourth-order, Runge–Kutta time-stepping scheme (Cox and Matthews 2002; Kassam and Trefethen 2005).² Time-averaged quantities are calculated by averaging the fields over the interval $30 \leq \mu t \leq 60$.

3. Results

a. Variation of the time-mean large-scale flow with wind stress forcing

Figure 2 shows how the time-mean, large-scale flow \bar{U} varies with wind stress forcing F for the two topographies. A generic feature of model (2), for both topographies used here (as well as other more complex and/or multiscale topographies) is the following: as wind stress strength varies from weak to stronger values, the flow transitions from a regime with relatively small time-mean, large-scale flow \bar{U} to a regime with large \bar{U} . Specifically, for very high wind stress forcing values, the time-mean, large-scale flow becomes $\bar{U} \approx F/\mu$, which is the value for \bar{U} in the flat-bottom case [cf. (2b) with $\eta = 0$]. The flat-bottom value F/μ is marked with the dashed–dotted line in both panels of Fig. 2. These two flow regimes are referred to as the lower branch and the upper branch (Davey 1980), and they are indicated in Fig. 2. In both branches, the flow reaches a steady state without any transients after an initial adjustment on the time scale of $O(\mu^{-1})$. For intermediate wind stress forcing values, the flow develops transients and becomes turbulent.

² A MATLAB code used for solving (2) is available at the github repository: https://github.com/navidcy/QG_ACC_1layer.

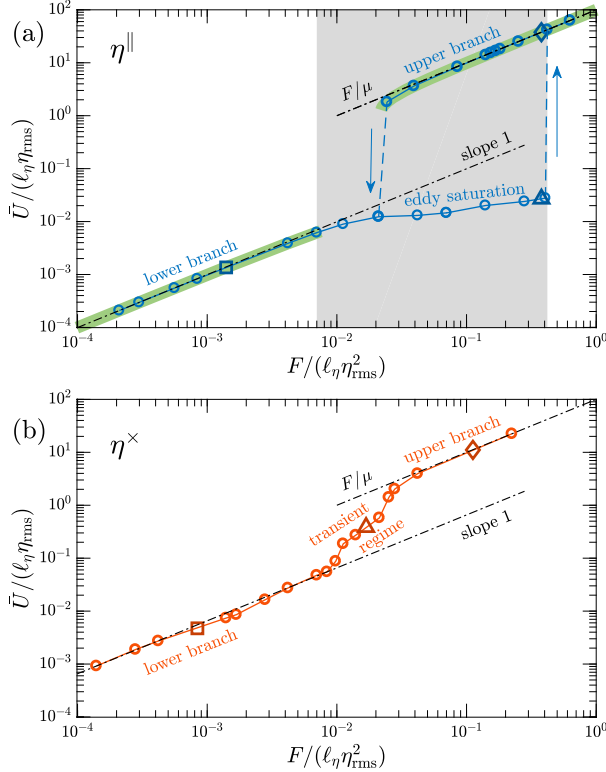


FIG. 2. The equilibrated, time-mean, large-scale flow \bar{U} as a function of the nondimensional forcing for the two topographies. (a) The case with open geostrophic contours; (b) the case with closed geostrophic contours. Dashed–dotted lines mark the slope 1 and the time-mean large-scale flow $\bar{U} = F/\mu$. In (a), the eddy saturation regime $7.0 \times 10^{-3} \leq F/(\ell_\eta \eta_{\text{rms}}^2) \leq 4.1 \times 10^{-1}$ is shaded. The thick semitransparent green curve marks the stability region of the steady solution (9). The points marked with a square \square , a triangle \triangle , and a diamond \diamond correspond to the three typical cases for which the energy spectra and flow field snapshots are shown in Figs. 4 and 5.

In the remainder of this subsection we describe in detail the qualitative features of the flow on the lower and upper branches as well as the transition from one branch to the other for the two topographies.

For weak wind stress forcing values (i.e., on the lower branch) the equilibrated solutions of (2) are time independent without any transient eddies. These steady states have a large-scale flow U and an associated stationary eddy flow field ψ that both vary linearly with wind stress forcing F . As a result, EKE varies quadratically with wind stress, that is, as F^2 . Figure 3a shows how EKE varies with wind stress forcing for topography η^{\parallel} and confirms the F^2 dependence on the lower branch (similar behavior is found for topography η^{\times} ; not shown). As the wind stress increases beyond a certain value, the lower-branch steady states undergo an instability and develop transients. Even though the

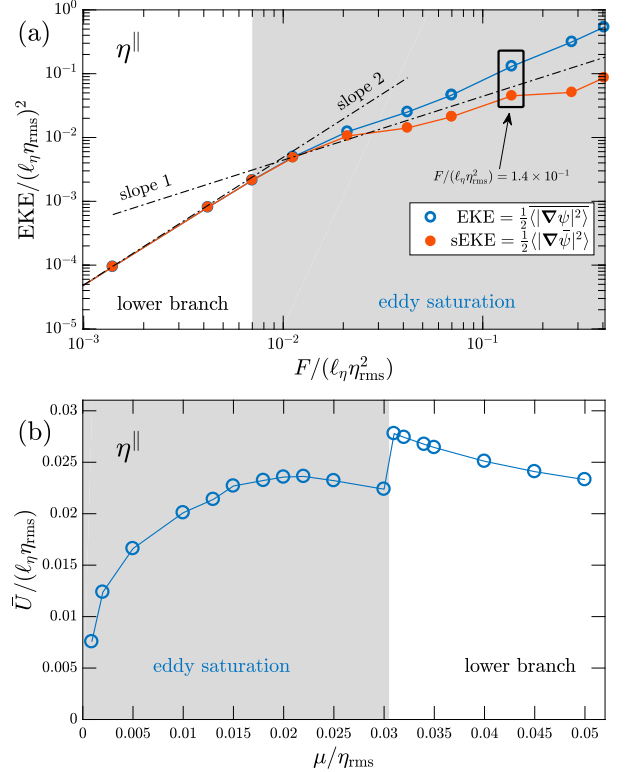


FIG. 3. (a) Variation of the equilibrated EKE and the standing eddy EKE (sEKE) with wind stress forcing for the topography η^{\parallel} , as the flow transitions from the lower branch to the eddy saturation regime. Dashed–dotted lines mark the slopes 1 and 2. (b) Variation of the equilibrated, time-mean, large-scale flow \bar{U} with bottom drag μ while wind stress forcing is kept constant at $F/(\ell_\eta \eta_{\text{rms}}^2) = 1.4 \times 10^{-1}$ [the value highlighted in (a)].

topography used here imposes a length scale ℓ_η , the transient eddies can have scales much smaller than ℓ_η . The onset of this instability is roughly at $F/(\ell_\eta \eta_{\text{rms}}^2) \approx 7.0 \times 10^{-3}$ for both topographies. (The stability of the lower-branch steady states for topography η^{\parallel} is studied in detail in section 5.)

For wind stress forcing values beyond the threshold of the lower-branch instability, the flow above the two topographies is qualitatively very different: topography η^{\parallel} shows eddy saturation, while topography η^{\times} does not (see Fig. 2).

For topography η^{\parallel} , as wind stress continues to increase beyond the onset of the transient eddy instability, the time-mean, large-scale flow \bar{U} ceases to grow linearly with F ; instead, \bar{U} grows at a much slower rate. In fact, \bar{U} shows only a very weak dependence on wind stress strength in the shaded region of Fig. 2a: \bar{U} increases only about fourfold in the course of a 60-fold wind stress increase from $F/(\ell_\eta \eta_{\text{rms}}^2) = 7.0 \times 10^{-3}$ up to 4.1×10^{-1} . This regime is identified as the eddy saturation regime.

The eddy saturation regime in Fig. 2a terminates at $F/(\ell_\eta \eta_{\text{rms}}^2) \approx 4.1 \times 10^{-1}$ by a discontinuous transition to the upper branch, marked with a dashed vertical line. The upper-branch steady solutions are characterized by much larger values of time-mean, large-scale flow \bar{U} compared to ones in the eddy saturation regime or on the lower branch. This discontinuous transition has been coined drag crisis (Constantinou and Young 2017). The location of the drag crisis exhibits hysteresis (Charney and DeVore 1979). As we increase wind stress forcing the drag crisis and the transition to the upper branch occurs at $F/(\ell_\eta \eta_{\text{rms}}^2) \approx 4.1 \times 10^{-1}$. However, if we initiate our model with the upper-branch solutions and start decreasing the wind stress forcing, we can find solutions on the upper branch down to $F/(\ell_\eta \eta_{\text{rms}}^2) \approx 2.44 \times 10^{-2}$ (see Fig. 2a). We note that to obtain the upper-branch solutions we have to be very delicate in initiating the system appropriately. Thus, although the upper-branch solutions shown in Fig. 2a are linearly stable, their basin of attraction is smaller than that of the coexisting eddy-saturated solutions. The extent of the region of multiple stable equilibria is explained by studying the stability of the upper-branch solution (see section 5).

On the other hand, the case with topography with closed geostrophic contours η^\times in Fig. 2b does not exhibit any drag crisis or any multiple equilibria. Also, the solutions using topography η^\times do not show any sign of eddy saturation; there is only a slight, barely noticeable decrease from the linear growth of the time-mean, large-scale flow \bar{U} in the range $8.0 \times 10^{-4} \leq F/(\ell_\eta \eta_{\text{rms}}^2) \leq 3.0 \times 10^{-3}$, and for those wind stress values the flow does not have any transient eddies. Transient eddies appear for wind stress forcing $F/(\ell_\eta \eta_{\text{rms}}^2) > 4.2 \times 10^{-3}$. For wind stress forcing values beyond the onset of transient eddies the flow transitions from the lower to the upper branch in a continuous manner between $F/(\ell_\eta \eta_{\text{rms}}^2) \approx 8.0 \times 10^{-3}$ and 4.2×10^{-2} and at a rate much faster than linear.

b. The flow regimes

As described in the previous subsection, we distinguish three qualitatively different flow regimes for each topography. There exist, for both topographies, a lower-branch flow regime for weak wind stress forcing and an upper-branch flow regime for strong wind stress forcing. These flow regimes consist of steady flows without any transient eddies. In between the lower- and upper-branch flow regimes there exists a regime in which the flow has a transient component: the eddy saturation regime for topography η^\parallel case and the transient regime for topography η^\times . These intermediate regimes are characterized by flows that feature strong transients and are turbulent, especially the eddy-saturated case. Moreover, in

these regimes the flow shows energy in a wide range of spatial scales. Figures 4 and 5 show the energy spectra and a snapshot of the flow fields for a typical representative case of each of the three flow regimes (the cases presented in Figs. 4 and 5 are the ones marked with a square; a triangle and a diamond in Figs. 2a and 2b).

The eddy field ψ in the eddy-saturated regime is characterized as two-dimensional turbulence. The wind stress F directly drives the large-scale flow U in (2b), and, in turn, U drives the eddy field through the term $U \partial_x \eta$ in (2a). This leads to a forward transfer of energy from the largest possible scale to the eddies on the length scale of the topography ℓ_n and then nonlinearity transfers energy from length scale ℓ_n to all other scales. This turbulent regime is anisotropic; for example, for the case marked with a triangle in Fig. 2a and also shown in Fig. 4c, the transient eddy velocities are related by $\langle u^2 \rangle \approx 0.57 \langle v^2 \rangle$. The turbulent eddy flow exhibits regimes that resemble the energy and enstrophy inertial ranges. For length scales smaller than ℓ_n , the energy spectrum even shows a slope close to -3 resembling the enstrophy inertial range as predicted by homogeneous isotropic turbulence arguments. Characteristically, for the open geostrophic contours case (Fig. 4) the eddy-saturated solution shows energy content in spatial scales other than ℓ_n that is at least eight orders of magnitude larger compared to the steady lower- and upper-branch solutions. Similar behavior is seen for the closed geostrophic contours case of Fig. 5. The difference between these two cases is that for topography η^\times the lower- and upper-branch solutions are not monochromatic, that is, they do not show energy content only at scale ℓ_n ; the nonlinearity caused by the nonvanishing Jacobian term $J(\psi, \eta^\times)$ induces energy to cascade to scales smaller than scale ℓ_n .

c. Further characteristics of the eddy saturation regime for topography η^\parallel

It has been noted that in the eddy saturation regime even though the total ACC transport varies very little with wind stress, the domain-averaged EKE is approximately linearly related to the wind stress (see, e.g., Hallberg and Gnanadesikan 2001, 2006). Figure 3a shows how this is reflected in this barotropic model; indeed, in the eddy saturation regime the EKE varies with wind stress forcing at a rate much slower than quadratic. It is also apparent from Fig. 3a that strong transient eddies characterize the eddy saturation regime; this can be seen by the diminishing of the standing eddy EKE (sEKE), that is, the EKE that results from the standing eddies alone.

The barotropic model (2) predicts that for a fully eddy-saturated state, that is, when \bar{U} does not vary at all

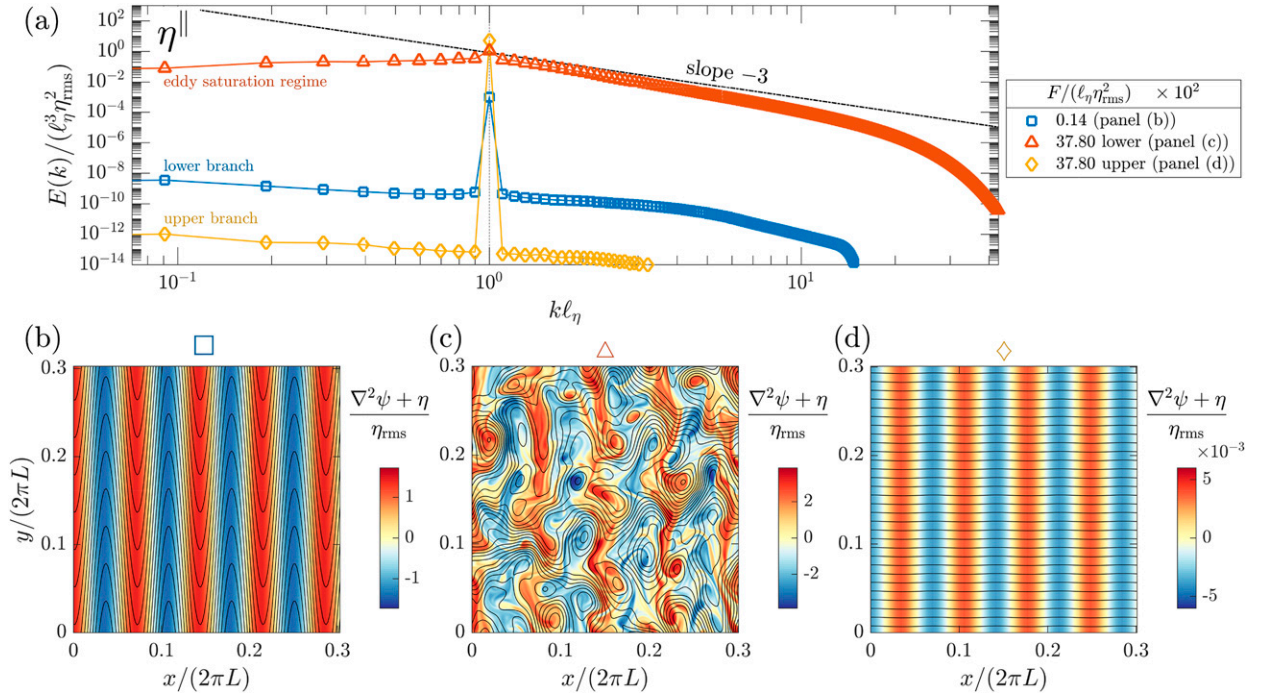


FIG. 4. (a) The energy spectra for three typical cases using topography η^{\parallel} with open geostrophic contours. The dashed-dotted line marks the slope -3 . (b)–(d) A final snapshot of the sum of the relative vorticity and the topographic PV, $\nabla^2\psi + \eta$ (colors) with the total streamfunction superimposed, and $\psi - Uy$ (contours) for each of the three cases presented in (a). [In (b)–(d) only a fraction of the flow domain is shown for better visualization.]

with F , the EKE should vary linearly with wind stress forcing. If the flow is completely saturated, then from (2b) we get that the form stress $\langle \bar{\psi} \partial_x \eta \rangle$ varies linearly

with F . With that in hand, we can understand why EKE varies linearly with wind stress from the energy power integral, that is, $\langle -\psi \times (2a) \rangle$ gives

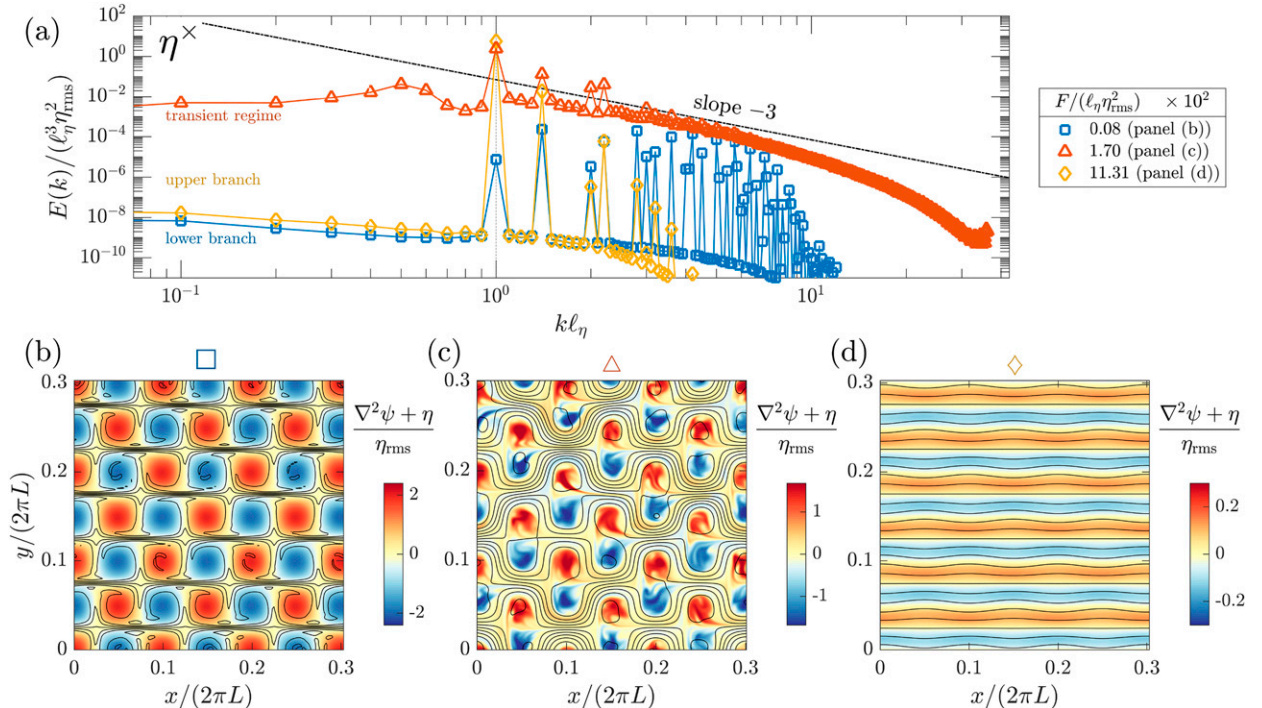


FIG. 5. As in Fig. 4, but for three typical cases using topography η^{\times} with closed geostrophic contours.

$$\overline{U} \langle \overline{\psi} \partial_x \eta \rangle + \underbrace{\overline{U'} \langle \psi' \partial_x \eta \rangle}_{\text{negligible}} = 2\mu \underbrace{\left\langle \frac{1}{2} |\nabla \psi|^2 \right\rangle}_{\text{def EKE}} + \text{small hyperviscous dissipation.} \quad (4)$$

If we consider the energy transfers among the various flow components, we deduce that $\overline{U'} \langle \psi' \partial_x \eta \rangle$ should be less than $\overline{U} \langle \overline{\psi} \partial_x \eta \rangle$ (Constantinou and Young 2017). Moreover, the numerical solutions of (2) suggest that in the eddy saturation regime the ratio of $\overline{U'} \langle \psi' \partial_x \eta \rangle$ to $\overline{U} \langle \overline{\psi} \partial_x \eta \rangle$ is less than about 10^{-3} and therefore negligible. Thus, (4) implies that EKE is proportional to form stress $\langle \overline{\psi} \partial_x \eta \rangle$, that is, EKE varies linearly with F .

Results both from quasigeostrophic models (Hogg and Blundell 2006; Nadeau and Straub 2012; Nadeau and Ferrari 2015) and also primitive equation models (Marshall et al. 2017) demonstrated the somehow counterintuitive fact that in the eddy saturation regime the total transport increases with increasing bottom drag. Hogg and Blundell (2006) suggested that this effect comes about because increasing the bottom drag decreases the strength of the transient eddies that are responsible for transferring momentum to the bottom where the topographic form stress acts; thus, the strength of the zonal current increases. Nadeau and Straub (2012) on the other hand, argued that increase of the bottom drag damps the gyre circulation and its associated form stress; thus, the zonal current increases to provide the drag needed to balance the momentum imparted by the wind stress.

In the barotropic model studied here, we also show that transport increases with increasing bottom drag in the eddy saturation regime. Figure 3b shows how the time-mean, large-scale flow \overline{U} varies when wind stress forcing is kept fixed at $F/(\ell_\eta \eta_{\text{rms}}^2) = 1.4 \times 10^{-1}$, while bottom drag μ varies; we find that \overline{U} increases with μ (up to a point). Here, the forcing is a steady, mean, zonal wind stress with no curl and thus large gyres do not form. Therefore, only the explanation by Hogg and Blundell (2006) can be applicable here. Within model (2) large bottom drag damps the eddy field ψ , thereby decreasing the form stress. Hence, increased bottom drag strengthens the time-mean, large-scale flow \overline{U} , which is necessary to balance the wind stress forcing F in the eddy saturation regime [cf. (2b)]. If we increase bottom drag μ beyond a certain threshold the flow becomes laminar and transitions from the eddy saturation regime to the lower-branch solution (for the case in Fig. 3b this transition occurs at $\mu/\eta_{\text{rms}} = 3 \times 10^{-2}$). On the lower branch the time-mean, large-scale flow \overline{U} decreases with increasing μ .

4. The effect of the transient eddies on the standing eddy field

The eddy PV fluxes

$$\mathbf{E} \stackrel{\text{def}}{=} \left(\overline{(U' + u') \nabla^2 \psi}, \overline{v' \nabla^2 \psi} \right), \quad (5)$$

appear as forcing in the standing eddy field $\overline{\psi}$. To elucidate how the zonal momentum balance is shaped by the transient eddies for the two different topographies, we compute the divergence of the eddy PV fluxes $\nabla \cdot \mathbf{E}$. Figure 6 compares the structure of the eddy PV flux divergence (shading) with the actual standing eddy field $\overline{\psi}$ (contours) for the two example cases with different topographies shown in Figs. 4c and 5c. There is an apparent qualitative difference between the two cases. For the open geostrophic contours case in Fig. 6a, the eddy PV fluxes are dominant over the whole domain, and, to a large extent, they are aligned with the standing eddy streamlines. This is not at all the case for the topography with closed geostrophic contours in Fig. 6b. In model (2) we can verify, by considering the energy budgets among components (Constantinou and Young 2017), that the only source of transient eddy energy is the energy conversion from the standing field component through the term $\langle \overline{\psi} \nabla \cdot \mathbf{E} \rangle$. Thus, the stronger the transient eddies are the stronger the correlation between eddy PV flux divergence and time-mean streamlines should be. In section 5 we show that for the case shown in Fig. 6a there is a strong transient eddy instability that explains this almost-perfect alignment between eddy PV fluxes and standing field streamlines.

More importantly, however, notice how for the case with $\cos(14x/L)$ topography shown in Fig. 6a, the eddy PV fluxes are offset from the topography contours by one-eighth wavelength (see Fig. 6c). This offset in the eddy forcing induces a standing flow that projects onto the $\sin(14x/L)$ rather than the $\cos(14x/L)$, that is, projects onto $\partial_x \eta^\parallel$ rather than η^\parallel . Since the time-mean topographic form stress is $\langle \overline{\psi} \partial_x \eta \rangle$, it is apparent that only the sin component of the standing eddy field can produce nonzero topographic form stress. Thus, the misalignment between the topography and the transient eddy forcing induces a standing eddy field that contributes to the form stress.

In conclusion, the transient eddies have the ability to shape the standing eddy field so that it projects more

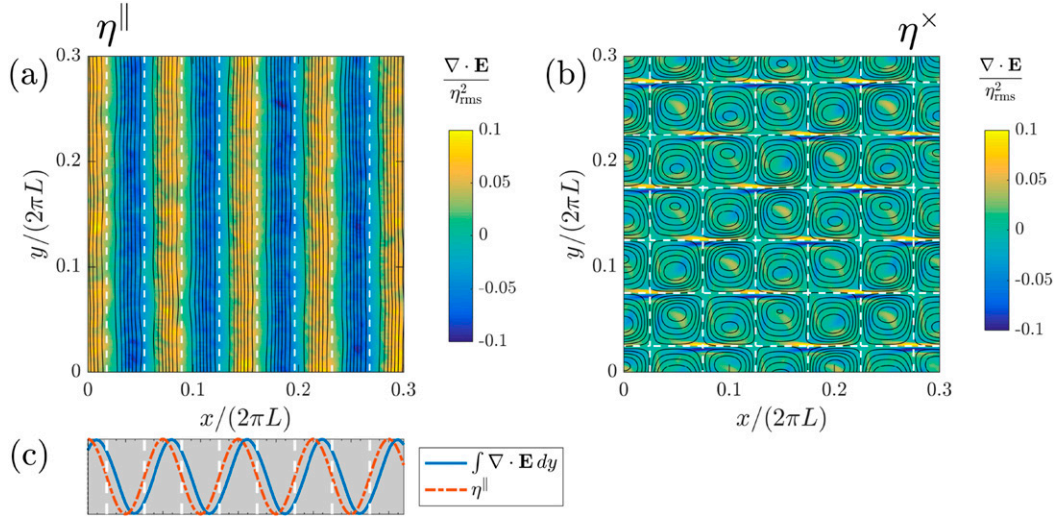


FIG. 6. (a),(b) A comparison of the eddy flux divergence $\nabla \cdot \mathbf{E}$ (shading) with the standing eddy streamlines $\bar{\psi}$ (black contours) for a case with topography (a) η^{\parallel} and a case with topography (b) η^{\times} . The cases shown correspond to the two examples marked with a triangle \triangle in Fig. 2 and also shown in Figs. 4c and 5c. For the open geostrophic contours case, the eddy PV fluxes dominate the whole domain and aligned with the mean flow streamlines. (c) Comparison of the normalized y -integrated eddy PV flux divergence with the topography for the case shown in (a). Notice how the eddy PV flux divergence is offset by one-eighth wavelength from the topography, thus exciting the $\sin(mx)$ component of the streamfunction. In all panels dashed white lines mark the $\eta = 0$ contour.

onto $\partial_x \eta$, therefore enhancing the time-mean topographic form stress. This shaping of the standing eddy field by the transient eddies is prominent in Fig. 6a with topography η^{\parallel} but not in the case with η^{\times} . Specifically, for the case shown in Fig. 6a the offset by one-eighth wavelength implies that $\nabla \cdot \mathbf{E}$ projects equally³ to both η and $\partial_x \eta$ (i.e., onto the cos and sin). Indeed,

$$\text{corr}(\eta^{\parallel}, \nabla \cdot \mathbf{E}) \approx \text{corr}(\partial_x \eta^{\parallel}, \nabla \cdot \mathbf{E}) = 0.69, \quad (6a)$$

where $\text{corr}(a, b) \stackrel{\text{def}}{=} \langle ab \rangle / \sqrt{\langle a^2 \rangle \langle b^2 \rangle}$. For topography η^{\times} in Fig. 6b these correlations are at least an order of magnitude less:

$$\text{corr}(\eta^{\times}, \nabla \cdot \mathbf{E}) = 0.01 \quad \text{and} \quad \text{corr}(\partial_x \eta^{\times}, \nabla \cdot \mathbf{E}) = -0.07. \quad (6b)$$

5. The stability of the lower- and upper-branch solutions for topography η^{\parallel}

For topography of the form $\eta = \eta_0 \cos(mx)$ [as is (3a)], we can understand both the transitions among the three flow regimes as well as the role that the transient eddies

play on eddy saturation by studying a three-dimensional invariant manifold of model (2).

It is easy to verify in this case that there exists a three-dimensional invariant manifold by assuming that the eddy streamfunction is

$$\psi = [S(t) \sin(mx) + C(t) \cos(mx)]/m. \quad (7)$$

Inserting (7) into (2), the Jacobian term $J(\psi, \eta)$ vanishes identically, and thus (2) reduces to

$$\frac{dC}{dt} = -\mu C + m(\beta/m^2 - U)S, \quad (8a)$$

$$\frac{dS}{dt} = -\mu S - m(\beta/m^2 - U)C - \eta_0 U, \quad \text{and} \quad (8b)$$

$$\frac{dU}{dt} = F - \mu U + \frac{1}{2} \eta_0 S, \quad (8c)$$

(after also ignoring ν_4 in D). Steady equilibrium solutions of (8) can be found in the form:

$$U = U^e, \quad \psi = \underbrace{[S^e \sin(mx) + C^e \cos(mx)]/m}_{\stackrel{\text{def}}{=} \psi^e}. \quad (9)$$

Both the lower- and upper-branch solutions for the case with topography η^{\parallel} are exactly such steady solutions in the form of (9) (see Figs. 4b,d).

Starting with the work by Hart (1979), the stability of solutions (9) to perturbations that lie within this invariant manifold has been extensively studied (Hart 1979;

³ A misalignment of one-eighth wavelength implies that both correlations in (6a) are $1/\sqrt{2}$.

Pedlosky 1981; Källén 1982; Rambaldi and Flierl 1983; Yoden 1985). Here, we study the stability of (9) to any general perturbation that may or may not lie within the invariant manifold. Charney and Flierl (1980) studied the stability of the inviscid and unforced version of (8), that is, with $\mu = F = 0$ and assuming the large-scale mean flow U^e to be a given external parameter of the problem. Here, we perform the stability of the forced–dissipative problem. Thus, we use U^e that results from a steady solution of (2) [or, for η^{\parallel} , a steady solution of (8)]. We investigate how this instability may elucidate why eddy saturation is observed.

a. Stability calculation

Assume perturbations about the steady state (9):

$$U(t) = U^e + \mathcal{U}(t), \psi(x, y, t) = \psi^e(x, y) + \phi(x, y, t) + [s(t) \sin(mx) + c(t) \cos(mx)]/m. \quad (10)$$

In (10), we write the perturbation streamfunction as a sum of a perturbation that lies within the three-state invariant manifold $[s \sin(mx) + c \cos(mx)]/m$ and a perturbation ϕ that does not project on the invariant manifold. That is, ϕ satisfies $\langle \phi e^{imx} \rangle = 0$.

By inserting (10) into (2) we get the linearized equations for the perturbations. When projected on the invariant manifold the perturbation equations read

$$\frac{dc}{dt} = -\mu c + m(\beta/m^2 - U^e)s - mS^e \mathcal{U}, \quad (11a)$$

$$\frac{ds}{dt} = -\mu s - m(\beta/m^2 - U^e)c - (\eta_0 - mC^e) \mathcal{U}, \quad \text{and} \quad (11b)$$

$$\frac{d\mathcal{U}}{dt} = -\mu \mathcal{U} + \frac{1}{2} \eta_0 s, \quad (11c)$$

while the orthogonal complement of the perturbation equations is

$$\partial_t \nabla^2 \phi = -[(U^e \nabla^2 + \beta) \partial_x + \mu \nabla^2] \phi - \{[S^e \cos(mx) - C^e \sin(mx)](\nabla^2 + m^2) + m\eta_0 \sin(mx)\} \partial_y \phi. \quad (12)$$

Eigenanalysis of (11) determines the stability of steady-state (9) to perturbations within the invariant manifold; eigenanalysis of (12) determines the stability of (9) to perturbations outside the manifold. Details for the eigenanalysis of (12) are provided in the appendix.

b. Stability results

The region of stability of steady states (9), both within and outside the low-dimensional manifold [i.e., with respect to

both (11) and (12)], is marked with the thick semitransparent curve in Fig. 2a. The onset of this barotropic–topographic instability explains (i) the appearance of transient eddies as wind stress is increased and (ii) the termination of the upper-branch solution as wind stress is decreased.

Figure 7a shows the large-scale flow U^e of the steady states (9) as a function of wind stress forcing F , together with their stability as predicted by (11) and (12). Also shown in Fig. 7a for comparison are the numerical results of (2). It is clear that the transition from the lower branch to the turbulent regime, in which eddy saturation is observed, is triggered by the instability caused by (12) rather than by (11). This instability of the lower branch first occurs at $F/(\ell \eta \eta_{\text{rms}}^2) = 7.15 \times 10^{-3}$. Figure 7c shows the most unstable eigenfunction just beyond the marginal point of instability. This eigenfunction has small-scale meridional structure; the meridional wavenumber of the eigenfunction shown in Fig. 7c is $n_y = 2.5m$. Thus, the instability of the lower branch caused by (12) introduces y dependence in the flow (see Fig. 7c).

Next, we would like to investigate how this instability contributes to the occurrence of eddy saturation. What is interesting here is how the instability maximum growth rate varies with the large-scale flow U^e . Figure 7b shows that in the regime in which we find eddy saturation the instability maximal growth rate caused by (12) increases dramatically with U ; growth rates increase by a factor of 1000 when U increases only by a factor of 15. The transient eddy source thus increases significantly for only small changes in U . In this way, and by analogy with arguments for baroclinic eddy saturation, larger wind stress forcing implies the need for stronger eddies, but much stronger eddies can be produced with just a slight increase in U^e , thus leading to eddy saturation. Furthermore, the above argument suggests that the flow adjusts to a state close to marginal stability for this barotropic–topographic instability, similarly to the baroclinic marginal stability argument first invoked by Stone (1978).

The stability calculations presented in this section are based on the fact that the topography does not depend on y . However, the same flow transitions occur for flows with open geostrophic contours above complex topographies. In that case, finding the lower- and upper-branch equilibrium steady states is much more painful since some of the Jacobian terms, for example, $J(\psi^e, \eta)$, are not identically zero. Therefore, the lower- and upper-branch solutions do not lie within any low-dimensional manifold. Methods for obtaining such equilibria were developed by Tung and Rosenthal (1985).

6. Discussion

The results reported here demonstrate that eddy saturation can occur even without baroclinicity. A bare barotropic setting is capable of producing an eddy

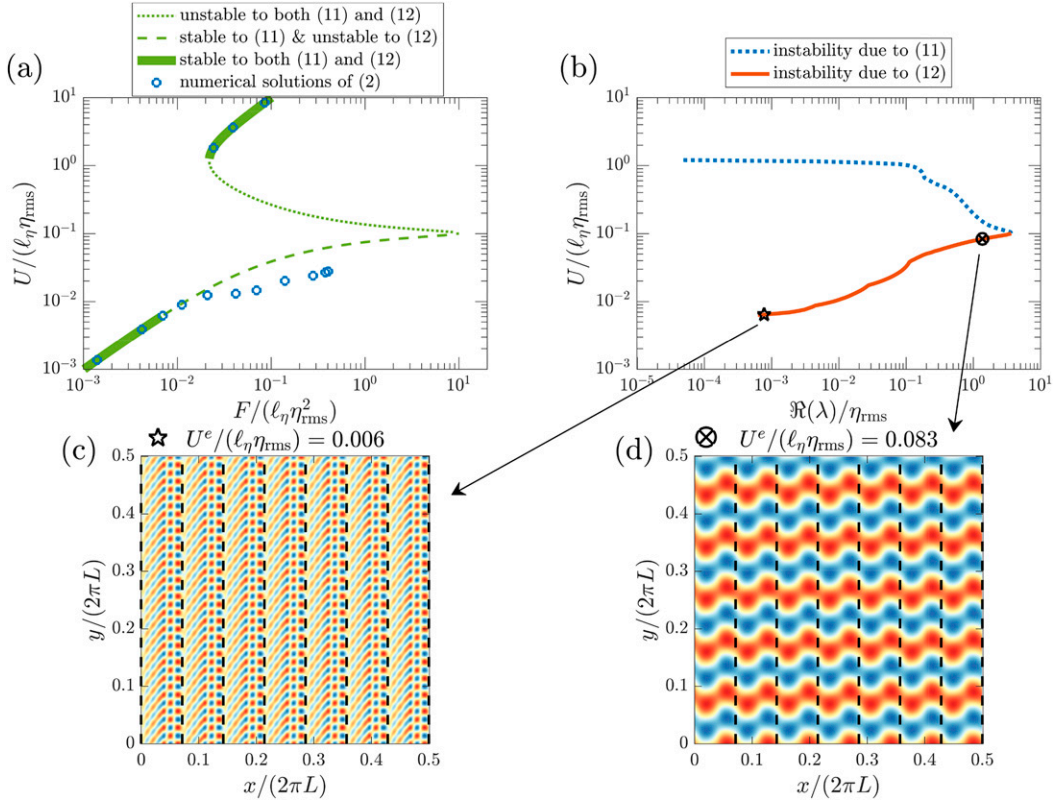


FIG. 7. (a) The steady solutions (9) for topography η^{\parallel} and their stability as predicted by (11) and (12). Also shown for comparison are the numerical solutions of (2) with circles. (b) The instability growth rates, that is, the real part of the eigenvalue λ . Only unstable eigenvalues are shown. (c) The structure of the most unstable eigenfunction that correspond to U^e just above the marginal point for instability. (d) The structure of the eigenfunction for U^e just before maximum instability. The eigenfunction in (c) has $n_y = 2.5m$ and Bloch wavenumber $n_x = m/2$; the eigenfunction in (d) has $n_y = m$ and Bloch wavenumber $n_x = 0$. The dashed black lines in (c) and (d) mark the topographic PV wavelength. Notice that only part of the domain is show for clarity. [The eigenfunctions were obtained with eigenanalysis of (A4).]

saturation regime in which the transport is insensitive to wind stress forcing. The model shows in addition some other features of eddy saturation that were previously observed in more elaborate ocean models; EKE varies close to linearly with wind stress forcing (instead of quadratically) and also transport increases with increasing bottom drag.

In this barotropic model with no baroclinic eddies, the flow relies on the barotropic–topographic instability to produce transient eddies. For the y -independent topography with open geostrophic contours η^{\parallel} , we extended the stability analysis of Hart (1979) to encompass any general flow perturbations. Thus, we managed to identify the various flow transitions shown in Fig. 2a with the onset of an instability. The stability calculations presented in section 5 crucially depend on the topography η^{\parallel} not depending on y . However, in the context of this barotropic model, we expect that the same flow transitions above more complex topography $\eta(x, y)$ with open geostrophic

contours would result from a similar barotropic–topographic instability. More importantly, by studying the barotropic–topographic instability we showed that for the case with eddy saturation the transient eddy source (i.e., the barotropic–topographic instability) had a particular property. The growth rate of the instability increases dramatically with small changes of the large-scale flow. This explains why eddy saturation occurs: an increase of the wind stress strength requires the generation of more transient eddies to carry this excess of momentum to the solid earth through form stress; but only a slight change in the transport can give rise to the transient eddies needed to balance the momentum. This is analogous with arguments for baroclinic eddy saturation.

The factor that controls the appearance or not of eddy-saturated states in a barotropic setting is whether or not the geostrophic contours are open. This was demonstrated here using two simple sinusoidal topographies that bare this distinction. However, the bare

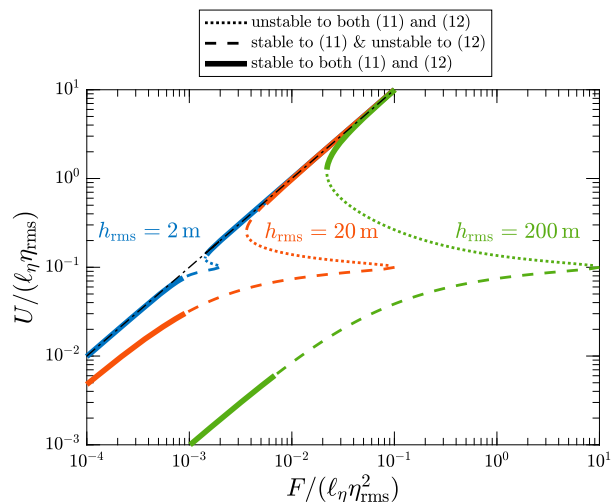


FIG. 8. Steady solutions (9) for topography η^{\parallel} with varying rms topographic height. Also shown is their stability as predicted by (11) and (12). The range of F values for which there is instability scales roughly as h_{rms}^2 . The dashed-dotted curve marks the flat-bottom solution F/μ .

existence of the eddy saturation in this simple setting depends on the presence of a transient eddy source (i.e., of an instability). The range of wind stress forcing values where eddy saturation could potentially occur is limited by the range of wind stress forcing values for which the barotropic–topographic instability occurs. The latter crucially depends on the height of the topography. For the flat-bottom case with $h = 0$, all geostrophic contours are open, but there is no eddy saturation since there is no instability. Figure 8 shows the steady states (9) together with their stability (similarly to Fig. 7a) for various topography heights. The range of wind stress forcing values that produces instability scales roughly as h_{rms}^2 .

We note that the flow characteristics that were described in section 3 are not quirks of the simple sinusoidal topographies in (3). The eddy saturation regime, the drag crisis, and multiple equilibria that are present here when geostrophic contours are open have been all also recently found to exist in this model for a flow above a random monoscale topography with open geostrophic contours (Constantinou and Young 2017) and also above a multiscale topography that has a k^{-2} power spectrum (not reported).

In conclusion, the results presented here emphasized that barotropic processes might play a role in shaping the zonal momentum balance in the ACC and in producing eddy saturation. In particular, barotropic processes are responsible at least for the component of the transport that is related to the bottom flow velocity of the ACC. [This bottom velocity component of the ACC transport accounts for about 25% of the total transport according to Donohue et al. (2016).] Even though the ACC is strongly affected by baroclinic processes, our results here reinforce the increasing evidence arguing for

the importance of the barotropic mechanisms in determining the ACC transport (Ward and Hogg 2011; Thompson and Naveira Garabato 2014; Youngs et al. 2017). Additionally, the results of this paper argue that topography does not only have a passive role in the momentum budget acting merely as a sink for zonal momentum, but it can also have an active role by producing transient eddies that shape the standing eddy field and its form stress.

Acknowledgments. I am mostly grateful to William Young for his support and insightful comments. Discussions with Anand Gnanadesikan, Petros Ioannou, Spencer Jones, Sean Haney, Cesar Rocha, Andrew Thompson, Gregory Wagner, and Till Wagner are greatly acknowledged. Also, I thank Louis-Philippe Nadeau and David Straub for their constructive review comments. This project was supported by the NOAA Climate and Global Change Postdoctoral Fellowship Program, administered by UCAR’s Cooperative Programs for the Advancement of Earth System Sciences. The author also acknowledges partial support from the National Science Foundation under Award OCE-1357047.

APPENDIX

Stability of Steady States (9) to Perturbations outside the Low-Dimensional Manifold

For the eigenanalysis of (12), first note that if ϕ is independent of y then (12) implies stability. Therefore, a necessary condition instability of (12) is $\partial_y \phi \neq 0$. In this case, also note that

- (i) (12) is homogeneous in y , that is, if $\phi(x, y, t)$ is a solution so is $\phi(x, y + a, t)$ for any a ; and
- (ii) the coefficients of (12) remain unchanged under $x \mapsto x + 2\pi\kappa/m$ for any integer κ , that is, if $\phi(x, y, t)$ is a solution so is $\phi(x + 2\pi\kappa/m, y, t)$.

Remark i implies that the linear operator in (12) commutes with the translation operator in y , and therefore they share the same eigenfunctions. Thus, the eigensolution has y -dependence $\propto e^{in_y y}$. Remark ii implies that the linear operator in (12) commutes with the appropriate translation operator by $2\pi\kappa/m$ in x , and thus the eigensolution has an x dependence in the form of a Bloch wavefunction.⁴ Therefore, we search for the eigensolutions of (12) as

$$\phi(x, y, t) = e^{\lambda t} e^{in_y y} \tilde{\phi}_{n_x}(x), \quad (\text{A1})$$

⁴For a more detailed discussion on Bloch eigenfunctions the reader is referred, for example, to the textbook by Ziman (1972) or to appendix D in the thesis of Constantinou (2015).

with

$$\tilde{\phi}_{n_x} \stackrel{\text{def}}{=} e^{in_x x} \sum_{M=-\infty}^{+\infty} c_M e^{iMmx}. \quad (\text{A2})$$

In (A1), it is understood that the eigenvalue λ depends on both n_x and n_y . In (A2), n_x is the zonal Bloch wavenumber, and it is restricted to take values $|n_x| \leq m/2$ (in condensed matter physics this is referred to as the first Brillouin zone). To see why n_x is restricted, consider what (A2) (or equivalently what remark ii) implies for the zonal spectral power of ϕ . Eigenfunction ϕ cannot have spectral power in any arbitrary zonal wavenumber but instead it can only have power at zonal wavenumbers:

$$\pm n_x, \pm(n_x \pm m), \pm(n_x \pm 2m), \dots \quad (\text{A3})$$

From (A3) we can verify that Bloch wavenumbers n_x and $\pm(n_x - m)$ are completely equivalent, and thus we only need to study the stability for $|n_x| \leq m/2$ (cf. Ziman 1972; Constantinou 2015).

With the ansatz (A1) the stability of (12) reduces to a generalized eigenvalue problem for each meridional wavenumber n_y :

$$\lambda \nabla_{n_y}^2 \tilde{\phi}_{n_x} = L_{n_y} \tilde{\phi}_{n_x}, \quad (\text{A4})$$

where $\nabla_{n_y}^2 \stackrel{\text{def}}{=} \partial_x^2 - n_y^2$ and

$$L_{n_y} \stackrel{\text{def}}{=} -[(U^e \nabla_{n_y}^2 + \beta) \partial_x + \mu \nabla_{n_y}^2] - in_y \{ [S^e \cos(mx) - C^e \sin(mx)] (\nabla_{n_y}^2 + m^2) + m\eta_0 \sin(mx) \}. \quad (\text{A5})$$

The problem is further reduced if we insert (A2) into (A4). Then, the eigenproblem (A4) reduces into an infinite system of equations whose unknowns are the coefficients c_M and the eigenvalue λ . Truncating the sum in (A2) up to $|M| \leq M_{\max}$ leaves us with $2M_{\max} + 1$ equations for $2M_{\max} + 2$ unknowns: $c_{-M_{\max}}, c_{-M_{\max}+1}, \dots, c_{M_{\max}}$ and λ . These equations are compactly written as

$$\mathbf{A}(\lambda) [c_{-M_{\max}}, \dots, c_{M_{\max}}]^T = 0, \quad (\text{A6})$$

where \mathbf{A} is a $(2M_{\max} + 1) \times (2M_{\max} + 1)$ matrix. A nontrivial solution of (A6) exists only when $\det[\mathbf{A}(\lambda)] = 0$, and this last condition determines the eigenvalues λ that correspond to the eigenfunction with wavenumbers n_x and n_y (Lorenz 1972; Gill 1974; Charney and Flierl 1980).

REFERENCES

Abernathy, R., and P. Cessi, 2014: Topographic enhancement of eddy efficiency in baroclinic equilibration. *J. Phys. Oceanogr.*, **44**, 2107–2126, <https://doi.org/10.1175/JPO-D-14-0014.1>.

Arbic, B. K., and G. R. Flierl, 2004: Baroclinically unstable geostrophic turbulence in the limits of strong and weak bottom Ekman friction: Application to midocean eddies. *J. Phys. Oceanogr.*, **34**, 2257–2273, [https://doi.org/10.1175/1520-0485\(2004\)034<2257:BUGITT>2.0.CO;2](https://doi.org/10.1175/1520-0485(2004)034<2257:BUGITT>2.0.CO;2).

Böning, C. W., A. Dispert, M. Visbeck, S. R. Rintoul, and F. U. Schwarzkopf, 2008: The response of the Antarctic Circumpolar Current to recent climate change. *Nat. Geosci.*, **1**, 864–869, <https://doi.org/10.1038/ngeo362>.

Bracegirdle, T. J., E. Shuckburgh, J.-B. Sallee, Z. Wang, A. J. S. Meijers, N. Bruneau, T. Phillips, and L. J. Wilcox, 2013: Assessment of surface winds over the Atlantic, Indian, and Pacific Ocean sectors of the Southern Ocean in CMIP5 models: Historical bias, forcing response, and state dependence. *J. Geophys. Res. Atmos.*, **118**, 547–562, <https://doi.org/10.1002/jgrd.50153>.

Bretherton, F. P., and M. Karweit, 1975: Mid-ocean mesoscale modeling. *Numerical Models of Ocean Circulation*, National Academy of Sciences, 237–249.

Carnevale, G. F., and J. S. Frederiksen, 1987: Nonlinear stability and statistical mechanics of flow over topography. *J. Fluid Mech.*, **175**, 157–181, <https://doi.org/10.1017/S002211208700034X>.

Charney, J. G., and J. G. DeVore, 1979: Multiple flow equilibria in the atmosphere and blocking. *J. Atmos. Sci.*, **36**, 1205–1216, [https://doi.org/10.1175/1520-0469\(1979\)036<1205:MFEITA>2.0.CO;2](https://doi.org/10.1175/1520-0469(1979)036<1205:MFEITA>2.0.CO;2).

—, and G. R. Flierl, 1980: Oceanic analogues of large-scale atmospheric motions. *Evolution of Physical Oceanography*, B. A. Warren and C. Wunsch, Eds., MIT Press, 504–549.

Constantinou, N., 2015: Formation of large-scale structures by turbulence in rotating planets. Ph.D. thesis, National and Kapodistrian University of Athens, 190 pp., <http://www.didaktorika.gr/eadd/handle/10442/35501?locale=en>.

—, and W. R. Young, 2017: Beta-plane turbulence above monoscale topography. *J. Fluid Mech.*, **827**, 415–447, <https://doi.org/10.1017/jfm.2017.482>.

Cox, S. M., and P. C. Matthews, 2002: Exponential time differencing for stiff systems. *J. Comput. Phys.*, **176**, 430–455, <https://doi.org/10.1006/jcph.2002.6995>.

Davey, M. K., 1980: A quasi-linear theory for rotating flow over topography. Part 1. Steady β -plane channel. *J. Fluid Mech.*, **99**, 267–292, <https://doi.org/10.1017/S0022112080000614>.

Donohue, K. A., K. L. Tracey, D. R. Watts, M. P. Chidichimo, and T. K. Chereskin, 2016: Mean Antarctic Circumpolar Current transport measured in Drake Passage. *Geophys. Res. Lett.*, **43**, 11 760–11 767, <https://doi.org/10.1002/2016GL070319>.

Farneti, R., T. L. Delworth, A. J. Rosati, S. M. Griffies, and F. Zeng, 2010: The role of mesoscale eddies in the rectification of the Southern Ocean response to climate change. *J. Phys. Oceanogr.*, **40**, 1539–1557, <https://doi.org/10.1175/2010JPO4353.1>.

—, and Coauthors, 2015: An assessment of Antarctic Circumpolar Current and Southern Ocean meridional overturning circulation during 1958–2007 in a suite of interannual CORE-II simulations. *Ocean Modell.*, **93**, 84–120, <https://doi.org/10.1016/j.ocemod.2015.07.009>.

Firing, Y. L., T. K. Chereskin, and M. R. Mazloff, 2011: Vertical structure and transport of the Antarctic Circumpolar Current in Drake Passage from direct velocity observations. *J. Geophys. Res.*, **116**, C08015, <https://doi.org/10.1029/2011JC006999>.

Gill, A. E., 1974: The stability of planetary waves on an infinite beta-plane. *Geophys. Astrophys. Fluid Dyn.*, **6**, 29–47, <https://doi.org/10.1080/03091927409365786>.

- Hallberg, R., and A. Gnanadesikan, 2001: An exploration of the role of transient eddies in determining the transport of a zonally reentrant current. *J. Phys. Oceanogr.*, **31**, 3312–3330, [https://doi.org/10.1175/1520-0485\(2001\)031<3312:AEOTRO>2.0.CO;2](https://doi.org/10.1175/1520-0485(2001)031<3312:AEOTRO>2.0.CO;2).
- , and —, 2006: The role of eddies in determining the structure and response of the wind-driven Southern Hemisphere overturning: Results from the Modeling Eddies in the Southern Ocean (MESO) project. *J. Phys. Oceanogr.*, **36**, 2232–2252, <https://doi.org/10.1175/JPO2980.1>.
- Hart, J. E., 1979: Barotropic quasi-geostrophic flow over anisotropic mountains. *J. Atmos. Sci.*, **36**, 1736–1746, [https://doi.org/10.1175/1520-0469\(1979\)036<1736:BQGF0A>2.0.CO;2](https://doi.org/10.1175/1520-0469(1979)036<1736:BQGF0A>2.0.CO;2).
- Hogg, A. M., and J. R. Blundell, 2006: Interdecadal variability of the Southern Ocean. *J. Phys. Oceanogr.*, **36**, 1626–1645, <https://doi.org/10.1175/JPO2934.1>.
- , M. P. Meredith, J. R. Blundell, and C. Wilson, 2008: Eddy heat flux in the Southern Ocean: Response to variable wind forcing. *J. Climate*, **21**, 608–620, <https://doi.org/10.1175/2007JCLI1925.1>.
- , —, D. P. Chambers, E. P. Abrahamson, C. W. Hughes, and A. K. Morrison, 2015: Recent trends in the Southern Ocean eddy field. *J. Geophys. Res. Oceans*, **120**, 257–267, <https://doi.org/10.1002/2014JC010470>.
- Holloway, G., 1987: Systematic forcing of large-scale geophysical flows by eddy-topography interaction. *J. Fluid Mech.*, **184**, 463–476, <https://doi.org/10.1017/S0022112087002970>.
- Johnson, G. C., and H. L. Bryden, 1989: On the size of the Antarctic Circumpolar Current. *Deep-Sea Res.*, **36A**, 39–53, [https://doi.org/10.1016/0198-0149\(89\)90017-4](https://doi.org/10.1016/0198-0149(89)90017-4).
- Källén, E., 1982: Bifurcation properties of quasigeostrophic, barotropic models and their relation to atmospheric blocking. *Tellus*, **34**, 255–265, <https://doi.org/10.3402/tellusa.v34i3.10809>.
- Kassam, A.-K., and L. N. Trefethen, 2005: Fourth-order time-stepping for stiff PDEs. *SIAM J. Sci. Comput.*, **26**, 1214–1233, <https://doi.org/10.1137/S1064827502410633>.
- Lorenz, E. N., 1972: Barotropic instability of Rossby wave motion. *J. Atmos. Sci.*, **29**, 258–269, [https://doi.org/10.1175/1520-0469\(1972\)029<0258:BIORWM>2.0.CO;2](https://doi.org/10.1175/1520-0469(1972)029<0258:BIORWM>2.0.CO;2).
- Mak, J., D. P. Marshall, J. R. Maddison, and S. D. Bachman, 2017: Emergent eddy saturation from an energy constrained parameterisation. *Ocean Modell.*, **112**, 125–138, <https://doi.org/10.1016/j.oceanmod.2017.02.007>.
- Marshall, D. P., J. R. Maddison, and P. S. Berloff, 2012: A framework for parameterizing eddy potential vorticity fluxes. *J. Phys. Oceanogr.*, **42**, 539–557, <https://doi.org/10.1175/JPO-D-11-048.1>.
- , M. H. P. Abbaum, J. R. Maddison, D. R. Munday, and L. Novak, 2017: Eddy saturation and frictional control of the Antarctic Circumpolar Current. *Geophys. Res. Lett.*, **44**, 286–292, <https://doi.org/10.1002/2016GL071702>.
- Marshall, G. J., 2003: Trends in the southern annular mode from observations and reanalyses. *J. Climate*, **16**, 4134–4143, [https://doi.org/10.1175/1520-0442\(2003\)016<4134:TITSAM>2.0.CO;2](https://doi.org/10.1175/1520-0442(2003)016<4134:TITSAM>2.0.CO;2).
- Masich, J., T. K. Chereskin, and M. R. Mazloff, 2015: Topographic form stress in the Southern Ocean State Estimate. *J. Geophys. Res. Oceans*, **120**, 7919–7933, <https://doi.org/10.1002/2015JC011143>.
- Meredith, M. P., A. C. Naveira Garabato, A. M. Hogg, and R. Farneti, 2012: Sensitivity of the overturning circulation in the Southern Ocean to decadal changes in wind forcing. *J. Climate*, **25**, 99–110, <https://doi.org/10.1175/2011JCLI4204.1>.
- Morrison, A. K., and A. M. Hogg, 2013: On the relationship between Southern Ocean overturning and ACC transport. *J. Phys. Oceanogr.*, **43**, 140–148, <https://doi.org/10.1175/JPO-D-12-057.1>.
- Munday, D. R., H. L. Johnson, and D. P. Marshall, 2013: Eddy saturation of equilibrated circumpolar currents. *J. Phys. Oceanogr.*, **43**, 507–532, <https://doi.org/10.1175/JPO-D-12-095.1>.
- Munk, W. H., and E. Palmén, 1951: Note on the dynamics of the Antarctic Circumpolar Current. *Tellus*, **3**, 53–55, <https://doi.org/10.3402/tellusa.v3i1.8609>.
- Nadeau, L.-P., and D. N. Straub, 2009: Basin and channel contributions to a model Antarctic Circumpolar Current. *J. Phys. Oceanogr.*, **39**, 986–1002, <https://doi.org/10.1175/2008JPO4023.1>.
- , and —, 2012: Influence of wind stress, wind stress curl, and bottom friction on the transport of a model Antarctic Circumpolar Current. *J. Phys. Oceanogr.*, **42**, 207–222, <https://doi.org/10.1175/JPO-D-11-058.1>.
- , and R. Ferrari, 2015: The role of closed gyres in setting the zonal transport of the Antarctic Circumpolar Current. *J. Phys. Oceanogr.*, **45**, 1491–1509, <https://doi.org/10.1175/JPO-D-14-0173.1>.
- , D. N. Straub, and D. M. Holland, 2013: Comparing idealized and complex topographies in quasigeostrophic simulations of an Antarctic Circumpolar Current. *J. Phys. Oceanogr.*, **43**, 1821–1837, <https://doi.org/10.1175/JPO-D-12-0142.1>.
- Pedlosky, J., 1981: Resonant topographic waves in barotropic and baroclinic flows. *J. Atmos. Sci.*, **38**, 2626–2641, [https://doi.org/10.1175/1520-0469\(1981\)038<2626:RTWIBA>2.0.CO;2](https://doi.org/10.1175/1520-0469(1981)038<2626:RTWIBA>2.0.CO;2).
- Peña Molino, B., S. R. Rintoul, and M. R. Mazloff, 2014: Barotropic and baroclinic contributions to along-stream and across-stream transport in the Antarctic Circumpolar Current. *J. Geophys. Res. Oceans*, **119**, 8011–8028, <https://doi.org/10.1002/2014JC010020>.
- Rambaldi, S., and G. R. Flierl, 1983: Form drag instability and multiple equilibria in the barotropic case. *Nuovo Cimento*, **6C**, 505–522, <https://doi.org/10.1007/BF02561449>.
- Rintoul, S. R., S. Sokolov, M. J. M. Williams, B. Peña Molino, M. Rosenberg, and N. L. Bindoff, 2014: Antarctic Circumpolar Current transport and barotropic transition at Macquarie Ridge. *Geophys. Res. Lett.*, **41**, 7254–7261, <https://doi.org/10.1002/2014GL061880>.
- Stone, P. H., 1978: Baroclinic adjustment. *J. Atmos. Sci.*, **35**, 561–571, [https://doi.org/10.1175/1520-0469\(1978\)035<0561:BA>2.0.CO;2](https://doi.org/10.1175/1520-0469(1978)035<0561:BA>2.0.CO;2).
- Straub, D. N., 1993: On the transport and angular momentum balance of channel models of the Antarctic Circumpolar Current. *J. Phys. Oceanogr.*, **23**, 776–782, [https://doi.org/10.1175/1520-0485\(1993\)023<0776:OTTAAM>2.0.CO;2](https://doi.org/10.1175/1520-0485(1993)023<0776:OTTAAM>2.0.CO;2).
- Swart, N. C., and J. C. Fyfe, 2012: Observed and simulated changes in the Southern Hemisphere surface westerly wind-stress. *Geophys. Res. Lett.*, **39**, L16711, <https://doi.org/10.1029/2012GL052810>.
- Tansley, C. E., and D. P. Marshall, 2001: On the dynamics of wind-driven circumpolar currents. *J. Phys. Oceanogr.*, **31**, 3258–3273, [https://doi.org/10.1175/1520-0485\(2001\)031<3258:OTDOWD>2.0.CO;2](https://doi.org/10.1175/1520-0485(2001)031<3258:OTDOWD>2.0.CO;2).
- Thompson, A. F., and A. C. Naveira Garabato, 2014: Equilibration of the Antarctic Circumpolar Current by standing meanders. *J. Phys. Oceanogr.*, **44**, 1811–1828, <https://doi.org/10.1175/JPO-D-13-0163.1>.
- Thompson, D. W. J., and S. Solomon, 2002: Interpretation of recent Southern Hemisphere climate change. *Science*, **296**, 895–899, <https://doi.org/10.1126/science.1069270>.
- Tung, K.-K., and A. J. Rosenthal, 1985: Theories of multiple equilibria—A critical reexamination. Part I: Barotropic

- models. *J. Atmos. Sci.*, **42**, 2804–2819, [https://doi.org/10.1175/1520-0469\(1985\)042<2804:TOMEAC>2.0.CO;2](https://doi.org/10.1175/1520-0469(1985)042<2804:TOMEAC>2.0.CO;2).
- Ward, M. L., and A. M. Hogg, 2011: Establishment of momentum balance by form stress in a wind-driven channel. *Ocean Modell.*, **40**, 133–146, <https://doi.org/10.1016/j.ocemod.2011.08.004>.
- Yang, X.-Y., R. X. Huang, and D. X. Wang, 2007: Decadal changes of wind stress over the Southern Ocean associated with Antarctic ozone depletion. *J. Climate*, **20**, 3395–3410, <https://doi.org/10.1175/JCLI4195.1>.
- Yoden, S., 1985: Bifurcation properties of a quasi-geostrophic, barotropic, low-order model with topography. *J. Meteor. Soc. Japan*, **63**, 535–546, https://doi.org/10.2151/jmsj1965.63.4_535.
- Youngs, M. K., A. F. Thompson, A. Lazar, and K. J. Richards, 2017: ACC meanders, energy transfer, and mixed barotropic–baroclinic instability. *J. Phys. Oceanogr.*, **47**, 1291–1305, <https://doi.org/10.1175/JPO-D-16-0160.1>.
- Ziman, J. M., 1972: *Principles of the Theory of Solids*. 2nd ed. Cambridge University Press, 435 pp.